



Experimental and Theoretical Studies of the Isotope Exchange Reaction $D + H_3^+ \rightarrow H_2D^+ + H$

P.-M. Hillenbrand^{1,4} , K. P. Bowen¹ , J. Liévin², X. Urbain³ , and D. W. Savin¹ 

¹ Columbia Astrophysics Laboratory, Columbia University, New York, NY 10027, USA; p.m.hillenbrand@gsi.de, savin@astro.columbia.edu

² Service de Chimie Quantique et Photophysique, Université Libre de Bruxelles, B-1050 Brussels, Belgium

³ Institute of Condensed Matter and Nanosciences, Université catholique de Louvain, B-1348 Louvain-la-Neuve, Belgium

Received 2019 March 4; revised 2019 April 4; accepted 2019 April 4; published 2019 May 22

Abstract

Deuterated molecules are important chemical tracers of prestellar and protostellar cores. Up to now, the titular reaction has been assumed to contribute to the generation of these deuterated molecules. We have measured the merged-beams rate coefficient for this reaction as a function of the relative collision energy in the range of about 10 meV–10 eV. By varying the internal temperature of the reacting H_3^+ molecules, we found indications for the existence of a reaction barrier. We have performed detailed theoretical calculations for the zero-point-corrected energy profile of the reaction and determined a new value for the barrier height of ≈ 68 meV. Furthermore, we have calculated the tunneling probability through the barrier. Our experimental and theoretical results show that the reaction is essentially closed at astrochemically relevant temperatures. We derive a thermal rate coefficient of $< 1 \times 10^{-12} \text{ cm}^3 \text{ s}^{-1}$ for temperatures below 75 K with tunneling effects included and below 155 K without tunneling.

Key words: astrochemistry – ISM: molecules – methods: laboratory: molecular – molecular data – molecular processes

1. Introduction

Deuterated molecules are important chemical tracers of the interstellar molecular clouds where stars form. At the ~ 10 – 20 K temperatures typical of these environments, exoergic deuterium-substitution reactions go forward, but the endoergic hydrogen-substitution reverse reactions do not, due to the vibrational zero-point energy (ZPE) of a deuterated molecule lying below that of its H-bearing counterpart. This fractionation process explains why, in cold environments, the observed abundance ratios of deuterated molecules relative to their H-bearing analogs are orders of magnitude larger than the galactic D/H ratio. Since these findings became apparent, numerous astrochemical models have been developed to explain the observations (an incomplete list of models includes Millar et al. 1989; Rodgers & Millar 1996; Roberts & Millar 2000; Walmsley et al. 2004; Flower et al. 2006; Aikawa et al. 2012; Albertsson et al. 2013; McElroy et al. 2013; Sipilä et al. 2013; Kong et al. 2015; Lee & Bergin 2015; Majumdar et al. 2017).

A particularly important deuterated molecule for tracing the properties of the cold gas in star-forming regions is H_2D^+ . Once the particle density of the cloud reaches $\sim 10^6 \text{ cm}^{-3}$, heavy elements are predicted to freeze onto dust grains. H_3^+ and its isotopologues are predicted to become the dominant carriers of positive charge, a role normally played by metals such as S^+ and Fe^+ , along with C-, N-, and O-bearing molecules such as HCO^+ , H_3O^+ , and N_2H^+ (van der Tak 2006). However, H_3^+ and D_3^+ are not observable at such low temperatures as they have no dipole moment and lack a pure rotational spectrum. Conversely, H_2D^+ and D_2H^+ have dipole moments and a pure rotational spectrum that can be excited at these temperatures. For example, H_2D^+ has been observed in low-mass prestellar cores (Caselli et al. 2003; Vastel et al. 2004, 2006; Pagani et al. 2009; Friesen et al. 2010), low-mass protostellar cores (Stark et al. 1999; Caselli et al. 2008;

Friesen et al. 2014), low-mass young stellar objects (Stark et al. 1999; Brünken et al. 2014), and massive star-forming regions (Harju et al. 2006; Swift 2009; Pillai et al. 2012).

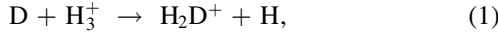
In order to harness the full diagnostic power of H_2D^+ for cold and dense star-forming regions, accurate chemical abundance models are needed. Measurements of the H_2D^+ abundance, combined with these models, can be used to determine the ionization fraction of the object. This fraction sets the timescale for the gas-phase chemistry of the gas, as ion-neutral reactions dominate such chemistry at these temperatures. Additionally, reliable values for the electron number density relative to the value of H_2 , $x_e = n_e/n_{H_2}$ are needed to calculate the electron-driven portion of the chemistry occurring in a cloud (Caselli et al. 2008). The quantity x_e is approximately equal to the ionization fraction, assuming that the gas is neutral. Lastly, the ionization and electron fractions determine the influence of magnetic fields on the dynamics of the object, especially for the ability of the ambient fields to support against gravitational collapse (van der Tak 2006; Grenier et al. 2015; Kong et al. 2015).

Of the six reactions identified as being key in the formation and destruction of H_2D^+ in cold and dense star-forming regions, two reactions involve HD, one involves D_2 , and two involve atomic D (Albertsson et al. 2013). Laboratory measurements exist for the reactions involving HD and D_2 (Adams & Smith 1981; Giles et al. 1992; Gerlich et al. 2002; Gerlich & Schlemmer 2002; Hugo et al. 2009), and the rate coefficients are thought to be well understood. The same cannot be said for the two reactions involving atomic D. This is due to the experimental challenges of generating controlled and well-quantified beams of atomic D (Bruhns et al. 2010a). Pagani et al. (2013) also highlighted the fact that reactions with atomic D have a sizable influence on the chemistry, especially at steady state when atomic D becomes important. These studies suggest that our ability to reliably use H_2D^+ as a diagnostic for star-forming regions is hindered by the lack of accurate

⁴ Present address: GSI Helmholtzzentrum für Schwerionenforschung, D-64291 Darmstadt, Germany.

astrochemical data for the reactions of atomic D with H_3^+ forming H_2D^+ and with H_2D^+ destroying the molecule.

Here we focus on the H_2D^+ formation reaction



which is exoergic by 51.51 meV (Ramanlal & Tennyson 2004). The only theoretical results published for this reaction appears to be the classical dynamics study by Moyano et al. (2004), which did not include corrections for the isotope-dependent ZPE along the reaction path. Their cross-section results lie an order of magnitude below the Langevin value. They hypothesized that this discrepancy might be reduced when quantum effects are taken into account. However, Moyano et al. also predicted that the reaction path possesses a barrier of $E_b = 149$ meV, and they did not account for the possible effects of tunneling. So, it is surprising that they report a nonzero cross section for collision energies below E_b .

To help to resolve this issue, we have carried out laboratory measurements for Reaction (1). The measurements were performed using our dual-source, ion-neutral, merged-fast-beams apparatus (O'Connor et al. 2015b; de Ruelle et al. 2016). In addition, we have carried out new theoretical calculations for the ZPEs for all of the stationary points along the reaction path, giving an improved value for E_b . Using our combined experimental and theoretical results, we have developed a semiempirical model for the reaction cross section, from which we have generated a thermal rate coefficient for Reaction (1) for astrochemical models.

The rest of the paper is organized as follows. In Section 2, we briefly describe the experimental apparatus. The measurement procedure and data analysis are highlighted in Section 3. Section 4 provides a theoretical description of the reaction path including the potential energy surface (PES) and the ZPE at all stationary points. The experimental results are presented in Section 5 and discussed in Section 6. A summary is given in Section 7. Throughout the paper, uncertainties are quoted at a confidence level taken to be equivalent to a one-standard-deviation statistical confidence level, unless otherwise noted.

2. Experimental Apparatus

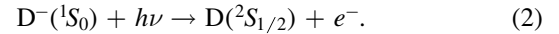
We have developed a dual-source, merged-fast-beams apparatus that enables us to study reactions between neutral atoms and molecular cations, and to measure the charged daughter products. The experimental apparatus and methodology have already been described in detail in O'Connor et al. (2015b) and de Ruelle et al. (2016). We provide here only a brief description, emphasizing aspects that are new or specific to the present study.

2.1. Neutral Beam

The neutral beam is formed by the photodetachment of a beam of D^- , the only bound level of which is $^1\text{S}_0$ (Rienstra-Kiracofe et al. 2002). The anions are generated using a Peabody Scientific duoplasmatron source, accelerated to form a beam with kinetic energy $E_{\text{D}^-} = 12.00$ keV (5.96 keV u^{-1} or 1.07×10^8 cm s^{-1}) and guided electrostatically into a Wien filter. This charge-to-mass filter is used to select the desired D^- beam and remove any other negatively charged particles extracted from the source. Typical D^- currents after the Wien filter were $3.7 \mu\text{A}$. The D^- beam is then directed into a

photodetachment chamber by a series of electrostatic ion optical elements.

In this chamber, the anions pass through a floating cell at a voltage of U_f . Upon entering this cell, the anions assume an energy of $E_{\text{D}^-} + eU_f$, where e is the elementary charge. Within the floating cell, a few percent of the anions are photodetached by a ~ 1 kW laser beam at a wavelength of $\lambda = 808$ nm (a photon energy of $h\nu = 1.53$ eV, where h is Planck's constant and ν the photon frequency). This energy lies close to the maximum of the photodetachment cross section (McLaughlin et al. 2017) and generates ground-level atomic D via



We have previously used this technique to produce beams of neutral atomic H and D for studies of associative detachment (Bruhns et al. 2010a, 2010b; Kreckel et al. 2010; Miller et al. 2011, 2012). Additional details can be found in O'Connor et al. (2015a).

The energy of the neutral beam formed is $E_n = E_{\text{D}^-} + eU_f$ and does not change upon leaving the floating cell. The beam is collimated by a set of two 5 mm apertures separated by a distance of 3168 mm, one before and one after the photodetachment chamber. The current before the first aperture was $3.3 \mu\text{A}$. The remaining D^- beam after the second aperture is electrostatically removed and directed into a beam dump, leaving a pure beam of ground-level D that continues ballistically into the interaction region.

2.2. Cation Beam

H_3^+ is generated using a Peabody Scientific duoplasmatron and extracted from the ion-source chamber through an aperture with a diameter of $d = 0.25$ mm. The cations are accelerated to form a beam of energy $E_{\text{H}_3^+} = E_i = 18.02$ keV or 5.96 keV u^{-1} . This energy has been selected to velocity match that of the neutral D beam for $U_f = 0$ V. The beam then passes through a Wien filter to select the desired H_3^+ and remove all other cations extracted from the source. After the Wien filter, the H_3^+ beam is electrostatically directed into a set of two 5 mm collimating apertures separated by a distance of 3069 mm. The current before the first aperture is typically $\approx 7 \mu\text{A}$. The second aperture is followed by a 90° electrostatic cylindrical deflector. This deflector merges the cations onto the neutral beam (which passes through a hole in the outer plate of the deflector and then through the exit of the deflector into the interaction region). Electrostatic ion optics after the last collimating aperture and before this merging deflector are used to maximize the overlap between both beams in the interaction region.

It is well known that duoplasmatrons form H_3^+ ions that are internally excited. The lower limit for this excitation at ~ 300 K is due to the water-cooled walls of the duoplasmatron. The upper limit is the predicted dissociation temperature of ~ 4000 K for H_3^+ in thermal equilibrium (Kylänpää & Rantala 2011). Our previous studies of C and O reacting with H_3^+ inferred an internal temperature of ~ 2500 – 3000 K by comparing the measured thresholds for competing channels to those predicted theoretically (O'Connor et al. 2015b; de Ruelle et al. 2016).

Here we adjusted the source-operating conditions in order to vary the level of internal excitation. The parameters that we varied were the pressure inside the duoplasmatron chamber, the arc current, the magnet current, and the filament current. As we

will discuss in more detail in Section 5, the level of H_3^+ internal excitation was most sensitive to the source pressure p_s .

We estimated p_s from the pressure measured just outside the source chamber, p_o . The short distance between the source aperture and the turbomolecular pump on the system allows us to treat the problem as two chambers separated by an aperture. Using the fact that $p_s \gg p_o$, the basic formula of molecular flow through an aperture gives (O’Hanlon 2003)

$$p_s = p_o \frac{4S}{d^2} \sqrt{\frac{2m_{\text{H}_2}}{\pi k_{\text{B}} T}}. \quad (3)$$

Here, $S = 2201 \text{ s}^{-1}$ is the H_2 pumping speed of the turbomolecular pump, m_{H_2} is the H_2 mass, k_{B} is the Boltzmann constant, and $T = 300 \text{ K}$ is the gas temperature. Inserting these values into Equation (3) yields

$$p_s \approx 1 \times 10^4 p_o. \quad (4)$$

We operated the source at $p_o = (0.72\text{--}7.2) \times 10^{-5}$ Torr, with the gauge calibrated for reading H_2 . This corresponds to $p_s = 0.072\text{--}0.72$ Torr.

2.3. Interaction Region

The interaction region begins near the exit of the merger deflector, at $z = 0 \text{ mm}$, where z is the distance along the overlap of the two beams. The length of the interaction region is $L = 1215 \text{ mm}$ and is set by the location of the entrance electrode of an electrostatic chicane, described below. The profiles of the two parent beams are measured individually using rotating wire beam profile monitors (BPMs; Seely et al. 2008), one near the beginning of the interaction region at $z = 280 \text{ mm}$ and the other near the end at $z = 1090 \text{ mm}$. The measured profiles are used to calculate the mean overlap factor of the parent beams, $\langle \Omega(z) \rangle$, as well as the bulk angle between them, θ_{bulk} . A Faraday cup can be inserted between the two BPMs to measure the cation beam current. Typical ion currents at this point were $I_i \approx 1.1 \mu\text{A}$. For $U_f = 0 \text{ V}$, daughter H_2D^+ ions form in the interaction region with an energy given by the initial $E_{\text{H}_3^+} = 18.02 \text{ keV}$ plus $E_{\text{D}} = 12.00 \text{ keV}$ and minus the energy of the replaced H atom, $E_{\text{H}} = 6.01 \text{ keV}$, resulting in $E_{\text{H}_2\text{D}^+} = 24.01 \text{ keV}$.

2.4. Signal Detection

After the interaction region, the desired daughter products are separated from the parent beams by a series of electrostatic analyzers. Using electrostatics allows us to analyze charged particles based on their kinetic energies. The first analyzer is a chicane, consisting of a series of four pairs of parallel plate electrodes. These deflect the charged particles in the horizontal direction. For each pair of plates, ℓ , one was set to a voltage $+U_\ell$ and the other to $-U_\ell$. The orientation of the chicane deflection has been rotated 90° from the configuration used in O’Connor et al. (2015b) and de Ruelle et al. (2016).

In our previous work, we used the chicane to deflect the parent cation beam into a Faraday cup located after the first electrode, while guiding the product ions back onto the optical axis of the chicane, as defined by the neutral beam trajectory. However, the geometry of the Faraday cup location requires a large mass difference between the parent and product ions. This could not be fulfilled in the present experiment. So, the H_3^+ beam current, I_i , was measured at the beginning and end of

each setting of U_f during data acquisition, typically a 10 s interval. The current was measured by applying a suitable voltage to the entrance electrode of the chicane. At this voltage, the transmittance of the cation beam from the interaction region to the chicane Faraday cup was 100%. During the H_2D^+ signal-collection portion of the data-acquisition cycle, the voltage on the entrance electrode was set to transmit the product ions through the chicane.

The daughter H_2D^+ ions are directed by the chicane into the final analyzer. This consists of a series of three 90° cylindrical deflectors, each with a bending radius of $\approx 137 \text{ mm}$: a lower cylindrical deflector (LCD), a middle cylindrical deflector (MCD), and an upper cylindrical deflector (UCD). The outer plate for each cylindrical deflector was set to a voltage of $+U_\ell$ and the inner plate to $-U_\ell$. In contrast to our previous work, all three deflections are now arranged in one vertical plane. The LCD and MCD together form a bend of 180° and the UCD provides a 90° bend in the opposite direction. A slit with a gap of 5 mm is positioned at the focus at the exit of the MCD to help suppress any background. This background is due, in part, to H_3^+ ions that make their way out of the chicane and into the final analyzer. The rear deflector pair of the chicane is used to correct for slight misalignments of the beam perpendicular to the vertical deflection plane of the final analyzer. The transmittance from the interaction region to the exit of the UCD was measured at $T_a = 90\% \pm 5\%$ using a proxy cation beam at the energy of the signal ions and a Faraday cup after the exit of the UCD.

Product ions are counted after the exit of the UCD using a channel electron multiplier (CEM) with an efficiency of $\eta = 99\% \pm 3\%$. A repeller grid is located in front of the CEM and biased negatively to repel electrons. The geometric transmittance of this grid is $T_g = 90\% \pm 1\%$. Typical H_2D^+ signal count rates were $S \approx 20 \text{ s}^{-1}$. The voltages on the chicane exit electrode, LCD, MCD, and UCD were scanned to determine the optimal settings for signal collection. Representative scans are shown in Figure 1 for $U_f = 0 \text{ V}$.

The trajectory of the H_2D^+ products is determined by the voltages applied to the four deflector pairs of the chicane and the three deflectors of the final analyzer. During data acquisition, we typically scan U_f to vary E_r . This also varies $E_{\text{H}_2\text{D}^+}$, and the various deflector voltages must be scaled accordingly. Denoting the deflectors from the entrance electrode of the chicane to the UCD by U_ℓ , with $\ell = 1\text{--}7$, we scale U_ℓ versus U_f as

$$U_\ell(U_f) = U_\ell(0) \left(1 + \frac{eU_f}{E_0} \right). \quad (5)$$

Here, $E_0 = 24.01 \text{ keV}$ is the H_2D^+ energy for $U_f = 0 \text{ V}$. These settings were routinely confirmed with signal scans similar to those shown in Figure 1.

2.5. Neutral Current

The neutral D beam travels ballistically from the interaction region, through the chicane, into the entrance aperture of the LCD, through an exit hole in the outer plate of the LCD, and into the neutral detector. The transmission of the neutral beam from the interaction region to the neutral detector, dubbed the neutral cup (NC), is $T_n = 95\% \pm 3\%$, as measured using proxy ion beams.

The neutral particle current, I_n , is measured in amperes. The neutral beam strikes a target inside the neutral cup, which is

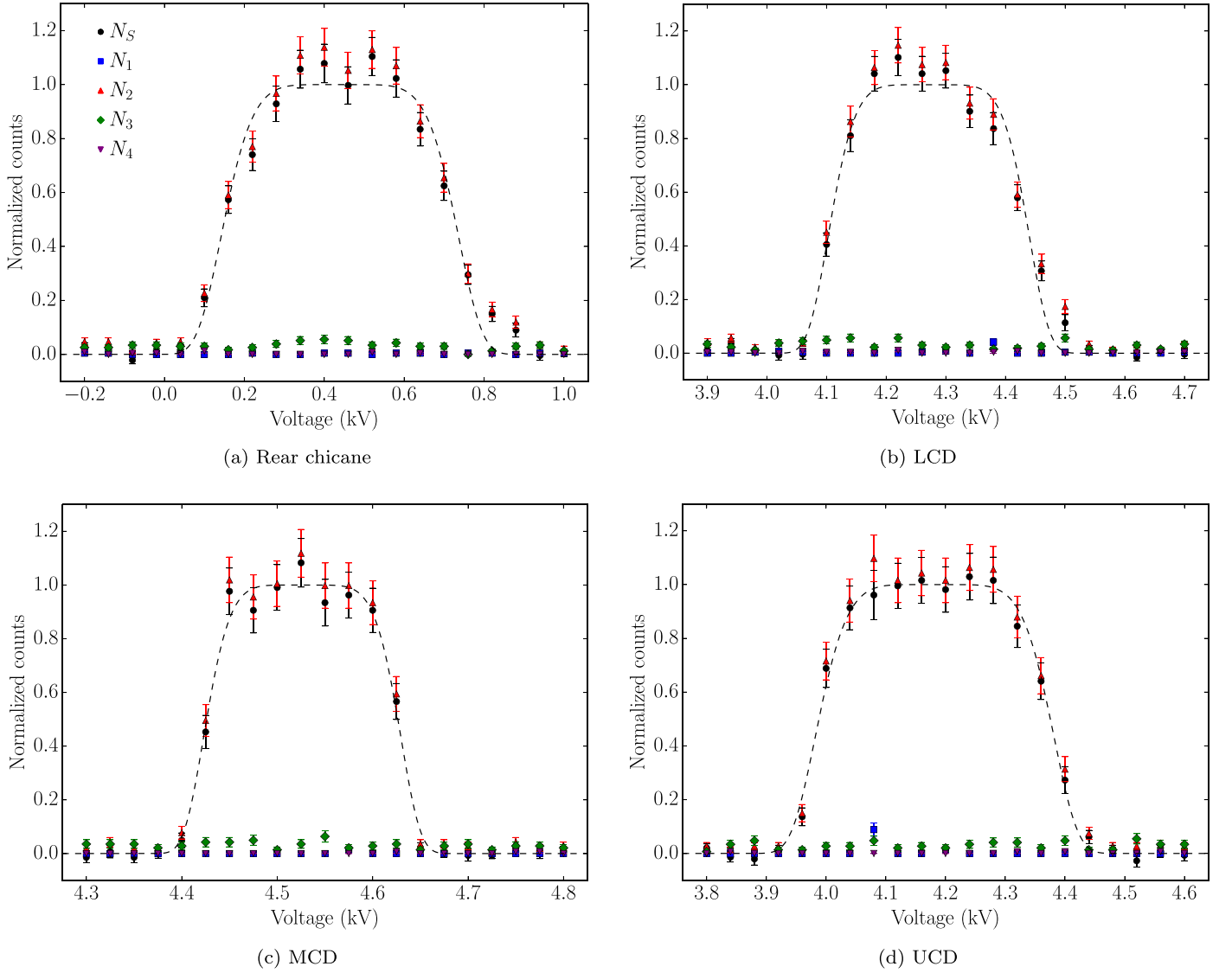


Figure 1. Voltage scans of the electrostatic analyzers for $U_f = 0$ V for the (a) rear deflector pair of the chicane, (b) LCD, (c) MCD, and (d) UCD. For these scans, each voltage was set to $|U_i| = 0.439, 4.271, 4.526,$ and 4.182 kV, respectively, when not being scanned. Shown are the normalized counts for the different phases of the measurement cycle, which provide unambiguous background subtraction. For N_1 (blue squares), only the D beam is on. For N_2 (red upward triangles), both beams are on. For N_3 (green diamonds), only the H_3^+ beam is on. For N_4 (purple downward triangles), both beams are off. The background-corrected signal (black circles) is given by N_5 (see Section 3.1). The dashed lines are normalized fits using a modified Gaussian function $\exp[-(U - U_0)^6 / (2\sigma^6)]$, where U is the applied voltage, U_0 the central voltage, and σ a fitting parameter. These fits are given as a guide to the eye.

configured to collect the resulting secondary emission of negative particles from the target (Bruhns et al. 2010b). This neutral cup can also be configured externally to serve as a Faraday cup for ion current measurements. The measured neutral current is given by

$$I_n = \frac{I_{NC}}{\gamma T_n}, \quad (6)$$

where I_{NC} is the negative particle current measured by the neutral cup and γ is the mean number of negative particles emitted by a neutral particle striking the target. For our work here, typical neutral D currents were $I_n = 43$ nA.

We measured the value of γ using collisional detachment of the D^- beam on a gas target, in this case the interaction region filled with Ar at a typical pressure of 6×10^{-4} Torr, using a pressure gauge calibrated for Ar. The resulting D beam was measured in the neutral cup. The remaining D^- beam was

deflected by the LCD into the MCD (which had no applied voltage), passed through a hole in the outer plate of the MCD, and was measured in a Faraday cup, dubbed the upper cup (UC). The transmittance of the D^- beam from the interaction region to the upper cup was measured to be $T_u = 65\% \pm 2\%$. Baseline measurements were also carried out for a residual gas pressure of 8×10^{-8} Torr, using the same Ar-calibrated gauge.

The resulting value of γ is given by

$$\gamma = \left(1 + \frac{\sigma_{DED}}{\sigma_{SED}}\right) \frac{\Delta I_{NC} T_u}{\Delta I_{UC} T_n}. \quad (7)$$

ΔI_{NC} and ΔI_{UC} represent the measured current changes in the neutral cup and upper cup, respectively. Each of these needs to be corrected for by the transmittance from the interaction region to the corresponding cup: T_n and T_u , respectively. We also accounted for the unmeasured D^+ cations generated by the

double electron detachment (DED) of D^- on Ar. The ratio of the DED cross section, σ_{DED} , compared to that for single electron detachment (SED), σ_{SED} , is $\sigma_{\text{DED}}/\sigma_{\text{SED}} = 3.5\%$. This is based on the compilation of Phelps (1992) and assumes that the cross sections for D^- on Ar are the same as those for H^- at matched velocities.

We measured γ over several measurement series spread out over a number of weeks and also for a range of values for E_n . At 12.00 keV, we found $\gamma = 1.6 \pm 0.1$. As a function of E_n , the data showed a small linear dependence of

$$\gamma(E_n[\text{keV}]) = 0.113E_n + 0.244 \quad (8)$$

within the energy range of $E_n = 11.1\text{--}13.0$ keV studied here. We accounted for this variation in the data analysis of our results.

3. Measurement and Analysis

We begin by explaining the signal determination (Section 3.1), followed by the data-acquisition procedure (Section 3.2), which has been enhanced since the work of O'Connor et al. (2015b) and de Ruelle et al. (2016). Next, we discuss the relative translational energy scale of the collision (Section 3.3). Then we review how we evaluate the corresponding merged-beams rate coefficient (Section 3.4). Again, we provide here only a brief description, emphasizing aspects that are new or specific to the present study. Additional details can be found in Bruhns et al. (2010b) and O'Connor et al. (2015b).

3.1. Signal Determination

In order to extract the desired signal, the two beams are chopped on and off, but out of phase with one another. This enables us to unambiguously subtract the various backgrounds. The chopping cycle is governed by the laser operating in a square-wave mode: on for 5 ms and then off for 5 ms. The H_3^+ beam is electrostatically chopped with the same time structure, but delayed by a phase shift of 2.5 ms. This chopping cycle is repeated for 10 s at a given value of U_f .

In the first phase of this chopping cycle, only the D beam is on and the counts are denoted by N_1 . In the second phase, both beams are on and the counts are N_2 . In the third phase, only the H_3^+ beam is on and the counts are N_3 . In the last phase, both beams are off and the counts are N_4 . The desired signal counts N_s are given by

$$N_s = N_2 - N_1 - N_3 + N_4 \quad (9)$$

and the corresponding statistical uncertainty by

$$\delta N_s = (N_1 + N_2 + N_3 + N_4)^{1/2}. \quad (10)$$

The signal rate S is given by dividing N_s by the corresponding integration time of $\tau = 2.5$ s at each step in the chopping pattern. The fractional statistical uncertainty in S is given by $\delta N_s/N_s$.

3.2. Data Acquisition Procedure

Each data run typically consists of 10 scans of U_f ($i = 1\text{--}10$), which is swept through a series of 20 voltage steps ($j = 1\text{--}20$) for each scan. A run corresponds to about one hour and is comparable to the timescale over which both beams are stable.

The U_f scan ranges used here were -900 to 1000 V, -450 to 500 V, and -225 to 250 V. Measurements of the ion and

neutral beam profiles are performed independently at the beginning and end of each sweep. For the neutral beam measurements, we found no significant variation over the range scanned in U_f . So, we set $U_f = 0$ V for the neutral beam profile measurements. The data presented below represent the average of various accumulated data runs over the three U_f ranges listed above.

Signal is collected within a predefined sweep range for U_f by automatically incrementing the floating cell voltage every 10 s. The voltages of the chicane and the final analyzer are scaled synchronously with each step of the floating cell voltage, as given by Equation (5). This configuration is to be contrasted with our earlier work where data were collected at just one floating cell voltage for each data run (O'Connor et al. 2015b; de Ruelle et al. 2016).

As mentioned earlier, it is not possible to set the voltages on the chicane to simultaneously direct the H_3^+ into the chicane Faraday cup and transmit the product H_2D^+ into the final analyzer. To overcome this, we measure the H_3^+ current, I_i , before and after each 10 s increment at a given U_f using the chicane Faraday cup as described earlier. We have confirmed that the ion beam is sufficiently stable over a 10 s increment to justify this.

3.3. Relative Translational Energy and Beam Overlap

The relative translational energy E_r in the center-of-mass system for monoenergetic beams intersecting at an angle θ is given by (Brouillard & Claeys 1983)

$$E_r = \mu \left(\frac{E_n}{m_n} + \frac{E_i}{m_i} - 2\sqrt{\frac{E_n E_i}{m_n m_i}} \cos \theta \right). \quad (11)$$

Here, $m_n = 2.015$ u and $m_i = 3.023$ u are the masses of the D atom and the H_3^+ ion, respectively (Linstrom & Mallard 2018). The reduced mass is defined as

$$\mu = \frac{m_n m_i}{m_n + m_i}. \quad (12)$$

For our work here, we have $\mu = 1.209$ u. The corresponding relative velocity is

$$v_r = \sqrt{\frac{2E_r}{\mu}}. \quad (13)$$

In our experiment, the two beams interact over a range of angles and with a spread in kinetic energies. The former is determined by θ_{bulk} between the two beams combined with the divergences of each beam. The latter is determined by the ± 10 eV energy spread of each source. We have calculated the resulting E_r using a Monte Carlo particle ray tracing as described in Bruhns et al. (2010b) and O'Connor et al. (2015b). These simulations were adjusted to match the constraints from the various collimating aperture dimensions and locations in the apparatus as well as from the measured beam profiles. Specifically, the simulations were adjusted to reproduce the measured typical bulk angle of $\theta_{\text{bulk}} = 0.39 \pm 0.19$ mrad, beam profiles, overlaps, and the overlap integral of $\langle \Omega(z) \rangle = 2.81 \pm 0.19 \text{ cm}^{-2}$, which was calculated from the beam profiles measured along the interaction region as described by Bruhns et al. (2010b) and O'Connor et al. (2015b).

The simulations also yield a histogram of relative translational energies throughout the interaction volume. We take the mean of this distribution as our experimental E_r and the one-standard-deviation spread of the histogram, ΔE_r , as our relative energy uncertainty. The resulting distribution of E_r for a given U_f is nearly Maxwellian for low values of $|U_f|$ and converges to a Gaussian distribution for larger values of $|U_f|$.

Additional fine-tuning of the E_r scale is achieved by comparing the results measured when the neutrals are faster than the ions ($U_f > 0$ V) to when they are slower ($U_f < 0$ V). The results should be symmetric in magnitude around $U_f = 0$ V. We find that the expected symmetry requires applying a small correction of $+6$ V to U_f . We attribute this to slight differences in the plasma potentials between the D⁻ and H₃⁺ duoplasmatron sources. Taking this into account in our simulations results in a calculated minimum experimental $E_r = 9 \pm 7$ meV, corresponding to a translational temperature of ≈ 70 K. The highest collision energies studied correspond to 10.8 ± 0.1 eV and 11.8 ± 0.1 eV for $U_f = -0.9$ kV and 1.0 kV, respectively.

3.4. Merged-beams Rate Coefficient

We measure the cross section, σ , for Reaction (1) times the relative velocity, v_r , between the colliders convolved with the energy spread of the experiment. The merged-beams rate coefficient and corresponding uncertainty for a given U_f scan i and voltage step j is given by

$$\langle \sigma v_r \rangle_{i,j} = \frac{N_{S_{i,j}} \pm \delta N_{S_{i,j}}}{\tau} \frac{1}{T_a T_g \eta} \frac{e^2 v_n v_i}{I_n I_i} \frac{1}{L \langle \Omega(z) \rangle}. \quad (14)$$

Here, the velocities v_n and v_i are those of the neutral and molecular ion beams, respectively, and are calculated using the corresponding beam energies. The other variables have been defined previously. We measure each of the quantities on the right-hand side of Equation (14), enabling us to generate absolute results, independent of any normalization.

Typical values of the experimental parameters going into Equation (14) and their uncertainties are summarized in Table 1. The neutral current is given by the average over the 10 s period j and the ion current by the average of the measurements before and after this period. $\langle \Omega(z) \rangle$ is taken from the average of all overlap measurements in a given data run, typically 11. Those quantities that varied between the steps of a scan are grouped under “Nonconstants” in Table 1 and those that remained constant throughout all runs are grouped under “Constants.”

In order to calculate $\langle \sigma v_r \rangle_j$ and the corresponding uncertainty for a given data run, we used the unweighted average of the results from all voltage scans i , given by

$$\langle \sigma v_r \rangle_j = \frac{\sum_{i=1}^{i_{\max}} \langle \sigma v_r \rangle_{i,j}}{i_{\max}}. \quad (15)$$

Various data runs were combined using a statistically weighted average of all measured $\langle \sigma v_r \rangle_j$ at the same U_f step (e.g., O’Connor et al. 2015b). Finally, the values of E_r and ΔE_r were assigned to each value of U_f , based on the average overlap and bulk angle from all data runs, as described in Section 3.3.

Table 1
Typical Experimental Values for Equation (14) with Corresponding Uncertainties

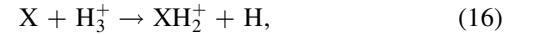
Source	Symbol	Value	Uncertainty (%)
<i>Nonconstants:</i>			
Signal rate (statistical)	S	20 s^{-1}	≤ 9
D velocity	v_n	$1.07 \times 10^8 \text{ cm s}^{-1}$	$\ll 1$
D current	I_n	43 nA	5
H ₃ ⁺ current	I_i	1.1 μ A	5
Overlap factor	$\langle \Omega(z) \rangle$	2.8 cm^{-2}	10
Neutral detector efficiency	γ	1.6	6
<i>Constants:</i>			
H ₃ ⁺ velocity	v_i	$1.07 \times 10^8 \text{ cm s}^{-1}$	$\ll 1$
Analyzer transmission	T_a	0.90	5
Grid transmission	T_g	0.90	1
Neutral transmission	T_n	0.95	3
CEM efficiency	η	0.99	3
Interaction length	L	121.5 cm	2
Total systematic uncertainty (excluding the signal rate)			15

Note. The total systematic uncertainty (excluding the statistical error) is calculated by treating each individual uncertainty as a random sign error and adding all in quadrature.

4. Theoretical Approach

4.1. Energy Profile of the Reaction Path

The six-dimensional Born–Oppenheimer (BO) electronic PES of the H₄⁺ cation defines the energy landscape governing the dynamics of the isotopic exchange reaction



where X = H or D.

For the X/H exchange reaction, a wave packet propagating on this PES will follow a route connecting the entrance channel to the exit channel. Along this path, the system will cross stationary points located on this surface (global/local minima and transition states). The relative energies of these critical points and the minimum energy path linking them define the BO-energy profile of the reaction. This profile is useful for discussing our experimental results and how they are affected by the presence of the potential energy barrier along the reaction path.

The height of the barrier with respect to the entrance channel corresponds to the minimum energy classically required to observe reactive trajectories. However, quantum mechanics requires that the total internal energy of the system be greater than or equal to its vibrational ZPE. It is therefore necessary to add the ZPE values of the different stationary points to the corresponding BO energies, leading to a vibrationally adiabatic minimum energy path (Jankunas et al. 2014). We refer to this below as the ZPE-corrected energy profile. The corrected barrier height can then be used to predict the minimum collision energy at which a nonzero cross section would be observed, in absence of quantum tunneling. Note that the BO

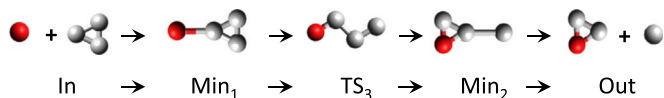


Figure 2. Molecular rearrangements along the minimum energy reaction path of the exchange reaction involving an X atom (H or D, shown in red) colliding with H_3^+ . The molecular plane is maintained along the entire path. See the text for details.

PES and the resulting energy profile are independent of the nuclear masses and are identical for the $X = \text{H}$ or D reactions. However, the corresponding ZPE-corrected profiles acquire the mass dependency of the vibrational energies and are thus not identical for $X = \text{H}$ and D .

Below, we determine the ZPE-corrected energy profiles from ab initio calculations. For this we build on previously published ab initio work characterizing the H_4^+ BO PES (Jiang et al. 1989; Álvarez-Collado et al. 1995; Moyano et al. 2004; Alijah & Varandas 2008; Sanz-Sanz et al. 2013).

4.2. Topography of the H_4^+ PES

The global topography of the H_4^+ PES is well known. The stationary points have been characterized (energies and geometries) at different levels of ab initio theory, and the convergence toward exact energies has been carefully investigated (Moyano et al. 2004; Alijah & Varandas 2008; Sanz-Sanz et al. 2013). Harmonic vibrational frequencies and the corresponding ZPE values have been calculated, but only for the H_4^+ isotopologue (Alijah & Varandas 2008; Sanz-Sanz et al. 2013). Global analytical PESs have also been interpolated from ab initio points, first by Moyano et al. (2004) at a medium level of theory and later by Sanz-Sanz et al. (2013) at a higher level. These calculations predict the energy path describing the X/H exchange reaction.

The successive molecular rearrangements occurring along the reaction coordinate during the exchange reaction are illustrated schematically in Figure 2. The X atom (H or D) collides with H_3^+ and forms an equilibrium structure, Min₁, in which X is weakly bound to the H_3^+ moiety. The X/H exchange is made possible by the transformation of Min₁ into a BO-equivalent minimum structure, Min₂, where X is now embedded into a triangular XH_2^+ structure, to which a H atom is weakly bound. This transformation implies the passage through a transition state, TS₃, using the nomenclature of previous works cited above. The dissociation of Min₂ leads to the final products of XH_2^+ and H. Note that the permutational symmetry arising from the identical hydrogen atoms of H_3^+ allows the wave packet to explore with an equal probability several pathways equivalent to the one depicted in Figure 2. As the permutational properties do not depend on X, it follows that both the H/H and D/H exchange reactions share the same pathways. However, as we show below, the ZPE-corrected energies are affected by the D/H isotopic substitution.

4.3. Ab Initio Results

The ZPE-corrected energy profiles for the $X = \text{H}$ and D reactions have been calculated using the ab initio theory carried out with the Molpro program package (Werner et al. 2012, 2015). The method we have used consists of a complete active space self-consistent field (CASSCF) calculation (Knowles & Werner 1985; Werner & Knowles 1985) followed

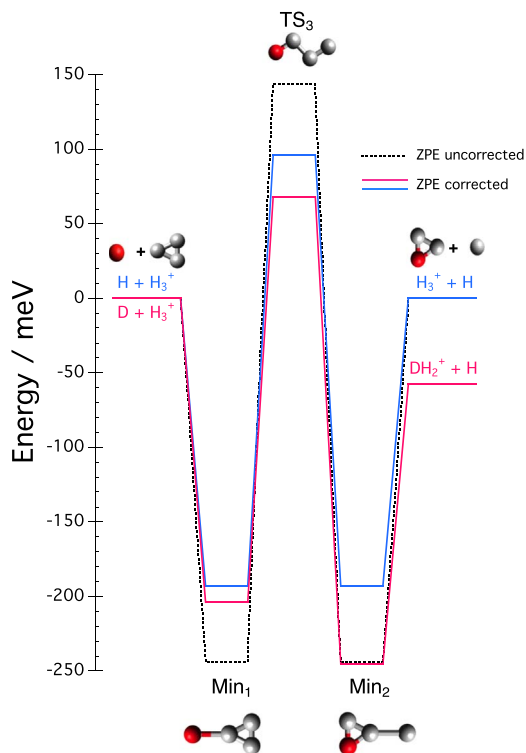


Figure 3. Our calculated energy profiles of the exchange reactions. The black dashed line is the BO-energy profile (ZPE uncorrected), and the colored lines correspond to the ZPE-corrected profiles (blue solid line for $X = \text{H}$ and red solid line for $X = \text{D}$). The molecular structures are shown at all stationary points, with the X atom colored in red. See the text for details.

by an internally contracted multireference configuration interaction (ic-MRCI) calculation (Knowles & Werner 1988; Werner & Knowles 1988). This highly correlated CASSCF/ic-MRCI approach was also adopted in previous works by Alijah & Varandas (2008) and Sanz-Sanz et al. (2013). For our work, we used a large active space including 16 molecular orbitals and the extended Dunning's augmented correlation-consistent polarized quintuple-zeta (aug-cc-pV5Z) basis set (Dunning 1989; Kendall et al. 1992), producing energies close to the corresponding full configuration interaction limit (within $2 \times 10^{-7} E_h$, where E_h is the Hartree energy). The equilibrium geometries and the harmonic vibrational frequencies of the different stationary points were calculated for the $X = \text{H}$ and D isotopologues.

Our results for the calculated energy profiles, one without the harmonic ZPE corrections and two with the corrections, are shown in Figure 3. The BO electronic energy for the entrance channel is the same for both $X = \text{H}$ and D . The corresponding $-1.8436004 E_h$ has been subtracted out and the difference expressed in meV, so as to better show the relative energy variations in the stationary points and the exit channel.

Table 2 gives the calculated energies for this energy profile, with the entrance energy subtracted out. Our calculated BO electronic energy for Min₁ and Min₂ is $-1.8525663 E_h$. For TS₃, it is $-1.8383087 E_h$. Our ZPE-uncorrected results are from the calculated ic-MRCI (16 active orbitals)/aug-cc-pV5Z energy differences. Our ZPE-corrected results add the ZPE energy differences to this, using the ZPE values given in Table 3 and the rotational ZPE for H_3^+ (as explained below). The barrier height, E_b , for Reaction (1) is highlighted in bold. Also given in Table 2 are the energies for both Min₁ and Min₂

Table 2
Characteristic Energies for the Profiles in Figure 3

Property		ZPE-uncorrected ^a	ZPE-corrected ^a	
			X = H	X = D
Potential well	Min ₁	−243.98	−193.19	−204.66
	Min ₂	−243.98	−193.19	−245.74
	Min _{1,2}	−239.41 ^b
	Min _{1,2}	−243.95 ^c
Barrier height	TS ₃	143.99	95.81	67.98
	TS ₃	149.25 ^b
	TS ₃	144.00 ^c
Exoergicity		0.00	0.00	−57.80
				−54.10 ^d
				−51.51 ^e

Notes. The potential well, barrier height, and exoergicity (all given in meV) correspond respectively to the energies of the minima, transition state, and exit channel, with respect to the entrance channel. The resulting barrier height, E_b , and the relative energy of the exit channel, ΔE_{zp} , are in bold.

^a From this work, unless otherwise specified.

^b From Moyano et al. (2004).

^c Calculated from Sanz-Sanz et al. (2013).

^d Includes the difference in electron binding energy for atomic H and D of 3.70 meV (Kramida et al. 2018), as was done by Ramanlal & Tennyson (2004).

^e From Ramanlal & Tennyson (2004).

from Moyano et al. (2004) and Sanz-Sanz et al. (2013), and the exoergicity from Ramanlal & Tennyson (2004).

The ZPE values have been derived using the vibrational frequencies ω_s for each oscillating mode listed in Table 3. The values of ω_s have been calculated using the harmonic oscillator approximation. Real values for ω_s are listed in order of increasing frequency. For TS₃, the corresponding imaginary frequency (ω_{im} discussed below) is given before the real ω_s values.

The number of normal modes of an N -atom nonlinear molecule is equal to $3N - 6$. Hence, there are six and three frequencies describing the vibrational motion of H_4^+ and H_3^+ , respectively. The energy for a vibrational level corresponding to the set of quantum numbers $v_1, v_2, \dots, v_{3N-6}$ is given, with respect to the bottom of the potential well, by the sum of the individual harmonic oscillator energies:

$$E(v_1, v_2, \dots, v_{3N-6}) = \sum_{s=1}^{3N-6} \hbar\omega_s \left(v_s + \frac{1}{2} \right). \quad (17)$$

This expression provides the ZPE value when all of the oscillators s are set to their $v_s = 0$ ground state, giving

$$E_{zp} = \frac{1}{2} \sum_{s=1}^{3N-6} \hbar\omega_s. \quad (18)$$

In order to calculate the ZPE for transition states, the summation in Equation (18) is limited to real frequencies. We also note that for H_3^+ , we use the rotational ZPE, which takes into account the fact that the $H_3^+(J = K = 0)$ ground rotational state is forbidden by the Pauli principle (Ramanlal & Tennyson 2004), where J is the rotational angular momentum quantum number and K is the projection of J along the symmetry axis of the system. The first allowed level, $J = K = 1$, lies 64.12 cm^{-1} above the nominal ground state

(Morong et al. 2009; Pavanello et al. 2012; Jaquet 2013). The rotational ZPE that we use here is the sum of the ground state ZPE and the energy of this first allowed level.

Particularly important for understanding Reaction (1) is TS₃. This is a first-order transition state and is thus characterized by a single imaginary frequency, ω_{im} , highlighted in bold in Table 3. The value of ω_{im} determines the negative curvature of the PES at the top of the reaction barrier. It is thus related to the barrier width and consequently to the tunneling probability, which we calculate in Section 6.4.2. The normal coordinate associated with ω_{im} for H_3D^+ is depicted in Figure 4, illustrating the reaction coordinate TS₃ that connects Min₁ and Min₂. Hydrogen atoms H_a and H_b are moving in parallel in the general direction toward the deuterium atom D, to form a triangular H₂D moiety. Meanwhile, hydrogen atom H_c travels in the opposite direction to form the elongated H_b–H_c bond of Min₂. Inverting the direction of the arrows leads to Min₁ on the other side of the barrier, with the formation of the H_aH_bH_c triangle and the elongated D–H_a bond.

Comparing our H_4^+ ZPE-uncorrected energies to the previously published ab initio calculations, we find excellent agreement with the work of Sanz-Sanz et al. (2013) using a similar level of theory, as shown in Table 2. This largely confirms the convergence of our MRCI expansion. We find poorer agreement with the results of Moyano et al. (2004). There are no previously published results for H_3D^+ for us to compare to our ZPE-corrected energies.

For the vibrational frequencies, we again find excellent agreement with the H_4^+ results of Sanz-Sanz et al. (2013), as can be seen in Table 3. The agreement is to within $<0.7 \text{ cm}^{-1}$, apart from a probable misprint for one of their frequencies for Min_{1,2} (see the footnote of Table 3). Larger discrepancies are observed compared to the calculations of Alijah & Varandas (2008), which were carried out using a smaller number of active orbitals. Even so, their results are only discrepant by $<2.7 \text{ cm}^{-1}$ for all frequencies, except for ω_{im} for TS₃, which differs by 7.6 cm^{-1} . Lastly, our frequencies for the H_3^+ isotopologues agree to within $<2.5 \text{ cm}^{-1}$ with the variational calculations of Lie & Frye (1992).

4.4. Further Theoretical Considerations

4.4.1. ZPE-corrected Profiles

The ZPE corrections to the characteristic energies of the collision profiles (see Table 2) are calculated with respect to the ZPE of the H_3^+ in the entrance channel. These corrections significantly alter the shape of the BO-energy profile, as shown in Figure 3. For X = H, the well depths and the barrier height are reduced by 21% and 33%, respectively. For X = D, the depth of Min₁ and the barrier height are reduced by 16% and 53%, respectively, but the depth of Min₂ is almost unchanged. These changes arise from the ZPE values, which are ordered for X = H as

$$E_{zp}(\text{Min}_1) = E_{zp}(\text{Min}_2) > E_{zp}(H_3^+) > E_{zp}(\text{TS}_3), \quad (19)$$

and for X = D as

$$E_{zp}(\text{Min}_1) > E_{zp}(H_3^+) \approx E_{zp}(\text{Min}_2) > E_{zp}(\text{TS}_3). \quad (20)$$

This ordering is a result of the decrease in the ZPE versus molecular structure. The ZPEs of the minima are high because

Table 3
Harmonic Vibrational Frequencies and Corresponding ZPE Values from Ab Initio Calculations

Structure	Property	Reference ^a	ZPE (cm ⁻¹) E_{zp}	Harmonic Frequencies (cm ⁻¹)					
				ω_1	ω_2	ω_3	ω_4	ω_5	ω_6
H ₄ ⁺	Min _{1,2}		4965.2	597.0	607.2	783.3	2221.6	2278.4	3442.8
	Min _{1,2}	Alijah & Varandas (2008)	4969	596	608	786	2224	2280	3443
	Min _{1,2}	Sanz-Sanz et al. (2013) ^b	4955	597	607	764 ^c	2221	2278	3443
	TS ₃		4167.0	942.4i	504.4	976.3	2009.0	2080.0	2764.3
	TS ₃	Alijah & Varandas (2008)	4168	950i	506	974	2011	2079	2765
	TS ₃	Sanz-Sanz et al. (2013) ^b	4167	942i	505	977	2009	2080	2764
H ₃ D ⁺	Min ₁		4872.7	476.9	581.5	762.4	2203.9	2277.9	3442.8
	Min ₂		4541.8	555.3	597.7	769.1	1961.4	2170.7	3029.5
	TS ₃		3942.5	875.9i	472.1	875.4	1908.0	2010.0	2619.5
H ₃ ⁺			4491.5	2773.2	2773.2	3436.5			
		Lie & Frye (1992)	4494.3	2774.9	2774.9	3438.8			
			4555.6 ^d						
H ₂ D ⁺			4089.4	2409.6	2533.6	3235.7			
		Lie & Frye (1992)	4088.9	2407.5	2533.4	3236.9			

Notes. The imaginary frequency of the transition state, ω_{im} , for Reaction (1) is marked in bold.

^a This work, unless otherwise specified.

^b See the supplementary material of this reference.

^c This value from Sanz-Sanz et al. (2013) is discrepant by 19 cm⁻¹ with respect to our value, while all of their other frequencies agree to within less than 1 cm⁻¹ with ours. This discrepancy is likely due to a misprint in their work, which also affects their corresponding ZPE value.

^d This is the rotational ZPE value, taking into account the rotational excitation of the first allowed H₃⁺ level, which lies 64.12 cm⁻¹ above the vibrational ZPE of 4491.5 cm⁻¹.

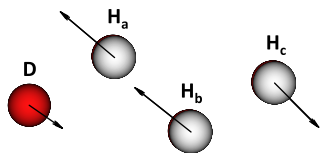


Figure 4. Atomic displacements of the mass-weighted normal mode coordinate of H₃D⁺ corresponding to the imaginary frequency ω_{im} of TS₃.

of the strong three-atom cycle, while those of the transition states are low, because of the weaker open structure. H₃⁺ is an intermediate case, with one fewer hydrogen, but it also has a strong three-atom cycle. Lastly, the case of Min₂ for X = D is fortuitous, a result of the deuteration effect, as explained below.

4.4.2. Effect of Deuteration

For X = H, the ZPE-corrected profile is symmetric with Min₁ and Min₂ being isoenergetic. But for X = D, the profile is asymmetric, with a potential well deeper for Min₂ than for Min₁. In general, the energy of the vibrational motions of the H₄⁺ isotopologues are decreased by deuteration. This can be seen in the reduction of the ZPE for the minima of H₃D⁺ compared to those for H₄⁺. The reduction is larger for Min₂, where the D atom affects the high-frequency vibrations of the three-atom cycle, than it is for Min₁, where the D atom acts on the low-frequency vibrations of the weak X–H bond. As a result, the ZPE value for Min₂ is fortuitously very close to the ZPE of H₃⁺. This explains the quasi-equality of the BO- and ZPE-corrected energies at the Min₂ position, as reported in Equation (20) and shown in Figure 3.

Deuteration also generates the exoergicity, ΔE_{zp} , of the X = D reaction. The resulting ΔE_{zp} , given in Table 2, is equal to the difference between the rotational ZPE for H₃⁺ and the ZPE for H₂D⁺.

4.4.3. Anharmonic and Nonadiabatic Effects

Our calculated energy profiles provide insight into the collision dynamics of the D + H₃⁺ reaction system. But to make the computations readily tractable, we have included neither the anharmonic effects in the ZPE calculations nor nonadiabatic corrections to the BO PESs. Still, these approximations are expected to have only a small effect on the calculated stationary energies and exoergicity, leading to only insignificant changes in our understanding of the reaction dynamics. The correction due to anharmonic effects amounts to 5% for the value of the ZPE difference between the H₃⁺ entrance channel and the H₂D⁺ exit channel, as estimated by comparing our exoergicity to the anharmonic results of Ramanlal & Tennyson (2004; see our Table 2). Nonadiabatic corrections to the BO PES are also estimated to be on the order of $\approx 10\%$. These corrections introduce nuclear mass effects that are ignored within the BO approximation. We expect that these would probably raise the barrier height slightly, as in the case of the H + H₂ reaction, where an increase of about 7 meV is observed together with a narrowing of the barrier (Mielke et al. 2005).

5. Merged-beams Rate Coefficient Results

Our measured $\langle\sigma v_r\rangle$ versus E_r is shown in Figure 5. The results are given for $E_r \approx 0.01$ –10 eV and for four different H₃⁺ source pressures. We attribute the decreasing trend from the highest $\langle\sigma v_r\rangle$ data set to the lowest to be due to decreasing levels of H₃⁺ internal excitation. As the fraction of internally excited H₃⁺ with energies sufficient to overcome E_b decreases, fewer ions can react and the measured $\langle\sigma v_r\rangle$ correspondingly decreases.

We varied the H₃⁺ internal excitation by adjusting the duoplasmatron operating parameters: source pressure, magnet

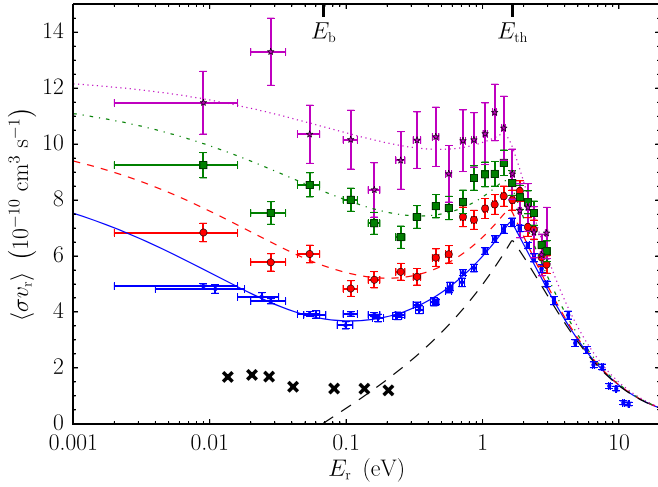


Figure 5. Merged-beams rate coefficient, $\langle\sigma v_r\rangle$, vs. the relative translational energy, E_r , for a range of H_3^+ source pressures, p_s . The vertical error bars represent the statistical uncertainty, and the horizontal error bars show the energy spread at each E_r . The data correspond to $p_s = 0.072$ Torr (purple stars), 0.72 Torr (green squares), 0.36 Torr (red large circles), and 0.48 Torr (blue small circles). The lines show the results of the model given in Section 6.2 with a fitted H_3^+ internal temperature of 4400 K (purple dotted line), 2510 K (green dotted-dashed line), 1610 K (red short-dashed line), and 1140 K (blue solid line). The black long-dashed line is the inferred result for 0 K. The black crosses show the theoretical data of Moyano et al. (2004). Vertical markers on the energy axis show the barrier height, E_b , given in Table 2, and the threshold of the first competing channel, E_{th} , given in Section 6.1.

current, filament current, and arc current. Of these, p_s had the biggest influence on the measured $\langle\sigma v_r\rangle$. Variations in the magnet and filament currents around the typical operating conditions of 0.45 A and 12 A, respectively, had only a minor effect. There was some influence of the arc current on $\langle\sigma v_r\rangle$, but the variation was small between a setting of 1 A and our typical operating condition of 0.75 A.

The observed dependence of the H_3^+ internal excitation on source pressure can be understood by considering the behavior of $\langle\sigma v_r\rangle$ versus p_s , as shown in Figure 6 for $E_r = 54 \pm 10$ meV. This collision energy is just below E_b . Classically, $\langle\sigma v_r\rangle$ should be zero for cold H_3^+ . Taking tunneling into account, we expect $\langle\sigma v_r\rangle \lesssim 4 \times 10^{-11} \text{ cm}^3 \text{ s}^{-1}$ (see Section 6.4.2). However, we have measured $\langle\sigma v_r\rangle \gg 4 \times 10^{-11} \text{ cm}^3 \text{ s}^{-1}$. Clearly, the H_3^+ in our measurement is internally excited. We attribute this to the gas-phase formation mechanism for the H_3^+ , namely proton transfer between H_2^+ and H_2 , with at least one of the two being vibrationally excited. Previous theoretical and experimental studies into the formation of H_3^+ have found internal energies of ~ 0.5 –1 eV (as reviewed in O’Connor et al. 2015b).

As for the pressure dependence shown in Figure 6, initially $\langle\sigma v_r\rangle$ decreases with increasing p_s . We attribute this to collisions between H_3^+ and H_2 in the source that cool the H_3^+ . This collisional cooling increases with increasing source pressure. Similar behavior has been seen in experimental photodissociation studies, which found generally decreasing levels of internal excitation with increasing source pressure (X. Urbain 2019, private communication). Then, at $p_s \sim 0.5$ Torr, $\langle\sigma v_r\rangle$ begins to increase with increasing source pressure. We attribute this to collisional re-excitation of the accelerated H_3^+ as it passes through the residual gas downstream of the source. As p_s increases, so does the H_2 streaming out of the duoplasmatron extraction aperture. This increases the residual gas pressure downstream of the source, enabling collisional re-excitation to

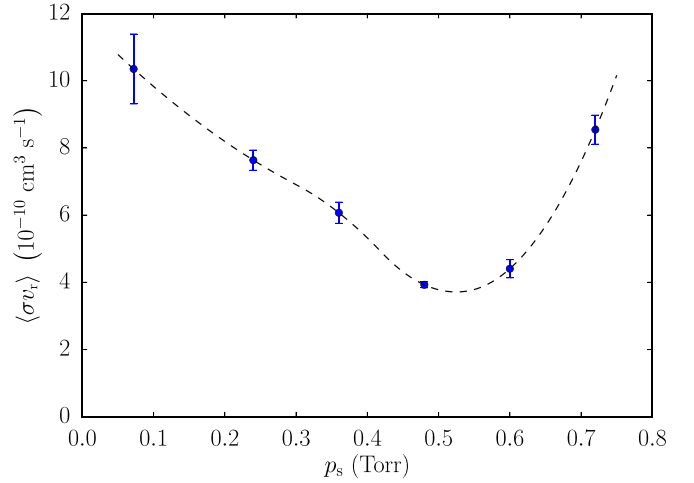


Figure 6. Experimental merged-beams rate coefficient, $\langle\sigma v_r\rangle$, for $E_r = 54 \pm 10$ meV vs. the pressure p_s inside the H_3^+ source. Shown are the measured data points with statistical error bars. The dashed line is a quadratic interpolation of the data, included to guide the eye.

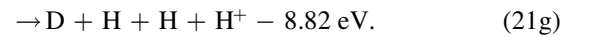
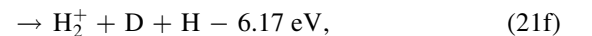
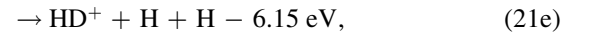
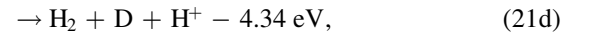
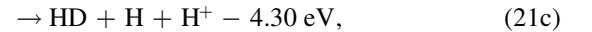
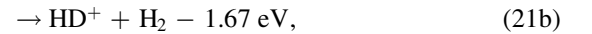
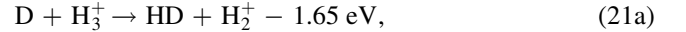
become important. A similar mechanism has been proposed by Kreckel et al. (2010) to explain the heating of H_3^+ ions accelerated from a supersonic expansion ion source.

Clearly, there is a minimum level of internal excitation of H_3^+ which can be achieved with our current experimental configuration. A setting of $p_s \approx 0.48$ Torr appears to provide the lowest level of internal excitation for our H_3^+ ions. The corresponding results are shown by the blue data points in Figure 5 and listed in Table 4.

6. Discussion

6.1. Competing Channels

There are no exoergic channels to compete with Reaction (1). All of the competing channels are endoergic. Up to the atomization limit, these include



The threshold energies for these exoergic channels have been calculated using the dissociation energy of H_3^+ from Jaquet (2013), the dissociation energies of diatomic molecules tabulated by Huber & Herzberg (1979), and the atomic electron binding energies of Kramida et al. (2018).

These competing channels explain one of the most dramatic features of our measured merged-beams rate coefficient, namely the rapid decrease starting near the threshold for the first two competing Channels 21(a) and (b). We define this energy as $E_{th} = 1.65$ eV. A similar behavior at the opening up of competing channels was seen in our earlier measurements of $\text{C} + \text{H}_3^+$ (O’Connor et al. 2015b) and $\text{O} + \text{H}_3^+$ (de Ruelle et al. 2016). As for the yet-higher-energy endoergic Channels 21(c)–(g), we see no clear change in the energy-dependent behavior

Table 4

List of Experimental Merged-beams Rate Coefficients, $\langle\sigma v_r\rangle$, with Corresponding One-standard-deviation Statistical Uncertainties, $\Delta\langle\sigma v_r\rangle$, as a Function of the Relative Translational Energy, E_r , with the One-standard-deviation Width of the Collision-energy Spread, ΔE_r , vs. Applied Floating Cell Voltages, U_f

U_f (kV)	E_r (eV)	ΔE_r	$\langle\sigma v_r\rangle$ ($10^{-10} \text{ cm}^3 \text{ s}^{-1}$)	$\Delta\langle\sigma v_r\rangle$
-0.900	10.774	0.120	0.754	0.066
-0.800	8.501	0.107	1.350	0.086
-0.700	6.506	0.093	2.112	0.102
-0.600	4.784	0.080	2.886	0.120
-0.500	3.333	0.066	4.404	0.145
-0.450	2.707	0.060	5.543	0.138
-0.400	2.148	0.053	6.377	0.111
-0.350	1.655	0.047	7.205	0.153
-0.300	1.227	0.040	6.604	0.113
-0.250	0.864	0.034	5.567	0.136
-0.225	0.707	0.031	5.059	0.154
-0.200	0.565	0.028	4.763	0.082
-0.175	0.440	0.025	4.358	0.143
-0.150	0.331	0.021	4.263	0.091
-0.125	0.238	0.018	3.861	0.136
-0.100	0.161	0.016	3.901	0.075
-0.075	0.099	0.013	3.521	0.129
-0.050	0.054	0.010	3.928	0.089
-0.025	0.024	0.008	4.543	0.146
0.000	0.009	0.007	4.918	0.083
0.025	0.011	0.007	4.820	0.152
0.050	0.028	0.008	4.383	0.094
0.075	0.060	0.011	3.905	0.137
0.100	0.108	0.013	3.930	0.075
0.125	0.172	0.016	3.782	0.136
0.150	0.251	0.019	3.891	0.089
0.175	0.345	0.022	4.079	0.139
0.200	0.454	0.025	4.359	0.079
0.225	0.579	0.028	4.908	0.156
0.250	0.719	0.031	5.402	0.104
0.300	1.045	0.037	6.179	0.111
0.350	1.430	0.043	6.968	0.153
0.400	1.876	0.049	6.988	0.118
0.450	2.381	0.055	5.932	0.145
0.500	2.946	0.061	5.003	0.102
0.600	4.251	0.073	3.889	0.140
0.700	5.788	0.084	2.642	0.122
0.800	7.556	0.096	2.033	0.103
0.900	9.550	0.108	1.262	0.834
1.000	11.769	0.119	0.710	0.064

Note. The data listed here correspond to the measurement, where the internal temperature of the H_3^+ inferred from our model is 1140 K.

of our results that would correspond to these channels opening up.

6.2. Cross-section Model for the Experimental Results

We have developed a semiempirical model to describe the experimental results shown in Figure 5. This model accounts for the dominant features seen in our measurements: the inferred reaction barrier, the varying levels of H_3^+ internal excitation, and the opening up of competing exoergic channels. We base our model, in part, on the Langevin-like formalism given by Levine (2005) for a scattering event with a reaction barrier. In this model, the cross section is given by $\sigma = \pi b^2$, where b is the maximum impact parameter for which the

reaction proceeds. In addition, all reactions are assumed to occur with a probability of unity for all impact parameters equal to or smaller than b .

For the first part of the model, we assume that any internal excitation energy, E_{int} , for a given level in H_3^+ is fully available to overcome any reaction barriers. Thus, the reaction will go forward when the sum of E_r and E_{int} is sufficient to overcome the combined energies of the repulsive centrifugal barrier and the reaction barrier. This gives

$$E_r + E_{\text{int}} \geq \frac{E_r b_b^2}{R_b^2} + E_b, \quad (22)$$

where b_b is the impact factor taking the reaction barrier into account and R_b is the radial separation of the reactants at the location of the reaction barrier. Solving for b_b^2 gives

$$b_b^2 \leq R_b^2 \left[1 + \frac{E_{\text{int}} - E_b}{E_r} \right]. \quad (23)$$

We take the maximum value of b_b^2 .

For the second part of the model, we introduce a flux reduction factor, $S(E_r, E_{\text{int}}, E_{\text{th}})$, to account for the opening of the competing exoergic channels discussed in Section 6.1. The value of E_r where the first competing channel opens up can be shifted from E_{th} toward lower energies by all or part of E_{int} , depending on the fraction, f , of E_{int} that goes into overcoming the threshold for the competing exoergic channel. By analogy with the so-called survival factor introduced for dissociative recombination studies by Strömholm et al. (1995), we can then write

$$S(E_r, E_{\text{int}}, E_{\text{th}}) = \begin{cases} 1 & E_r < E_{\text{th}} - fE_{\text{int}} \\ \frac{1}{[1 + a(E_r - E_{\text{th}} + fE_{\text{int}})]^2} & E_r \geq E_{\text{th}} - fE_{\text{int}}, \end{cases} \quad (24)$$

where a and f are adjustable parameters. Putting together everything so far, we have

$$\sigma_b(E_r, E_{\text{int}}) = \begin{cases} 0 & E_r + E_{\text{int}} < E_b \\ \pi R_b^2 \left[1 + \frac{E_{\text{int}} - E_b}{E_r} \right] S(E_r, E_{\text{int}}, E_{\text{th}}) & E_r + E_{\text{int}} \geq E_b. \end{cases} \quad (25)$$

Next, we take into account that the upper limit for a reaction cross section is commonly assumed to be the classical Langevin value, σ_L . The Langevin cross section results from the combined effects of the attractive charge-induced dipole moment between D and H_3^+ , and the repulsive centrifugal barrier, and is given by (Levine 2005)

$$\sigma_L(E_r) = \pi e \left(\frac{2\alpha_D}{E_r} \right)^{1/2}. \quad (26)$$

Here, α_D is the static dipole polarizability of D. This is given by Schwerdtfeger & Nagle (2019) as $\alpha_D = 9a_0^3 / (8\pi\epsilon_0)$, where a_0 is the Bohr radius and ϵ_0 is the vacuum permittivity.

Solving Equations (25) and (26), we find that for a given value of E_{int} , $\sigma_b > \sigma_L$ for E_r below some energy that we define as E_x . As E_{int} increases, so does the value of E_x . To avoid these situations, we select the reaction cross section to be the smaller of σ_b and σ_L . In addition, we assume complete scrambling of

the nuclei during the $D + H_3^+$ reaction. This is guided by the theoretical approach of Hugo et al. (2009) for isotopic variants of the $H_2 + H_3^+$ reaction. For the $D + H_3^+$ reaction, only three of the asymptotic channels lead to the formation of H_2D^+ . The fourth outgoing channel leads to the formation of H_3^+ . To account for this, we introduce a factor of 3/4 into our reaction cross section, giving

$$\sigma(E_r, E_{\text{int}}) = \frac{3}{4} \min[\sigma_b(E_r, E_{\text{int}}), \sigma_L(E_r)]. \quad (27)$$

Now, in order to compare this reaction cross section to our experimental results, we need to take into account the excitation energy of each H_3^+ level involved in the reaction. We do this assuming that the H_3^+ levels follow a Boltzmann distribution,

$$g(E_{\text{int}}) = \exp(-E_{\text{int}}/\langle E_{\text{int}} \rangle), \quad (28)$$

where $\langle E_{\text{int}} \rangle$ is a function of the internal temperature T_{int} of H_3^+ and is derived from the partition function $Z(T)$,

$$\langle E_{\text{int}} \rangle = k_B T_{\text{int}}^2 \frac{1}{Z} \frac{\partial Z}{\partial T_{\text{int}}}. \quad (29)$$

We use the parameterization of $\langle E_{\text{int}} \rangle$ versus T_{int} given in Kylänpää & Rantala (2011).

In the penultimate step of our model, we convolve Equation (27) over E_{int} . The resulting model cross section is given by

$$\begin{aligned} \sigma_{\text{mod}}(E_r, \langle E_{\text{int}} \rangle) \\ = \frac{1}{\langle E_{\text{int}} \rangle} \int_0^\infty \sigma(E_r, E_{\text{int}}) \exp(-E_{\text{int}}/\langle E_{\text{int}} \rangle) dE_{\text{int}}. \end{aligned} \quad (30)$$

There are four adjustable parameters in our model cross section: R_b , $\langle E_{\text{int}} \rangle$, a , and f . For the other values needed in Equation (30), we use $E_b = 67.98$ meV from our ab initio calculations (see Section 4.3) and $E_{\text{th}} = 1.65$ eV from the calculated energetics for the competing exoergic channels (see Section 6.1).

Lastly, in order to compare to our measured merged-beams rate coefficient, we multiplied Equation (30) by v_r and varied the four adjustable parameters to best fit the experimental data. Given the complexity of the model cross section and the lack of any clean analytic formula for the cross section, we carried out a by-eye fit, as opposed to a least-squares fit. This is not expected to be an issue as our model is overconstrained by the data. For $E \lesssim E_{\text{th}}$, the magnitude and energy dependence of the data are determined by R_b and $\langle E_{\text{int}} \rangle$. Having fixed those two parameters, we then fit for a and f using the data for $E_r \gtrsim E_{\text{th}}$. In each energy range, we fit for two free parameters using our four sets of measured data, thereby making the system overconstrained. As an additional constraint, we required that the fits all use the same set of values for R_b , a , and f , and only let $\langle E_{\text{int}} \rangle$ vary between the fits to the four data sets.

Our semiempirical model results are shown in Figure 5. The model clearly demonstrates all of the major energy dependencies seen in the experimental data, namely (i) a pronounced minimum in the merged-beams rate coefficient near $E_r \sim 0.1$ eV, (ii) a distinct increase in the merged-beams rate coefficient from this energy until the opening of the competing exoergic reaction channels, (iii) a subsequent rapid decrease in merged-beams rate coefficient, and (iv) an overall increase of the merged-beams rate coefficient with increasing $\langle E_{\text{int}} \rangle$ of H_3^+ .

Commenting on the best-fit parameters, we found the best agreement between the measured data and our model for $R_b = 2.53a_0$. This is relatively close to the geometry of TS_3 , which has a distance of $2.87 a_0$ between the D atom and the center of mass of the H_3^+ moiety, as deduced from the optimized geometry computed by Sanz-Sanz et al. (2013). The best-fit values of $\langle E_{\text{int}} \rangle$ for the various source conditions are 0.185, 0.32, 0.65, and 1.5 eV, corresponding to $T_{\text{int}} = 1140$, 1610, 2510, and 4400 K, respectively. The case where we attribute an internal temperature of 4400 K to the reacting H_3^+ illustrates the uncertainty in our model, as this temperature is beyond the calculated 4000 K dissociation limit of H_3^+ (Kylänpää & Rantala 2011). Nevertheless, the inferred range of H_3^+ temperatures is in reasonable agreement with previous estimates from our measurements of C and O reacting with H_3^+ (O'Connor et al. 2015b; de Ruelle et al. 2016). Finally, the fall-off in the merged-beams rate coefficient that starts near E_{th} is best fit with $a = 0.3$ and $f = 0.2$. The value for f suggests that 20% of E_{int} goes into overcoming the opening up of the competing exoergic channels, while 80% is transferred into the daughter products.

6.3. Comparison to Theoretical Cross Sections

The classical trajectory (CT) cross-section calculations of Moyano et al. (2004) for Reaction (1) are shown in Figure 5, multiplied by the values of v_r that correspond to their reported collision energies. Surprisingly, the CT data are nonzero below E_b . It appears that Moyano et al. have only taken into account the ZPE of the initial H_3^+ and have not accounted for the important ZPE changes along the reaction path. As a result, the reaction complex begins with sufficient energy to overcome the ZPE-uncorrected reaction barrier. This leads to the observed unphysical prediction in the low-energy reaction dynamics, an issue known as the ‘‘ZPE-leakage’’ problem that is encountered in CT and quasi-classical trajectory (QCT) simulations (Lu & Hase 1989; Guo et al. 1996). This probably explains the unphysical CT results of Moyano et al., who predicted a nonzero cross section at energies below E_b for both $X = H$ and D collisions.

Several different solutions for solving the ZPE leakage have been proposed (Guo et al. 1996; Lee et al. 2018, and references therein). Among these solutions, the ring-polymer molecular dynamics approach (Habershon et al. 2013) was recently applied with success to the $D^+ + H_2 \rightarrow HD + H^+$ reaction (Bhowmick et al. 2018). This could be an interesting alternative to CT or QCT calculations for Reaction (1).

6.4. Thermal and Translational Temperature Rate Coefficients

Using our semiempirical model cross section, we can generate rate coefficients for thermal conditions where the translational temperature of the gas, T_{gas} , and the internal temperature, T_{int} , are equal. However, the published theoretical rate coefficients are more appropriately compared to a translational temperature rate coefficient where $T_{\text{int}} = 0$ K. Here, we present both rate coefficients. We also present a theoretical correction to our thermal results to account for the effects of tunneling through the reaction barrier.

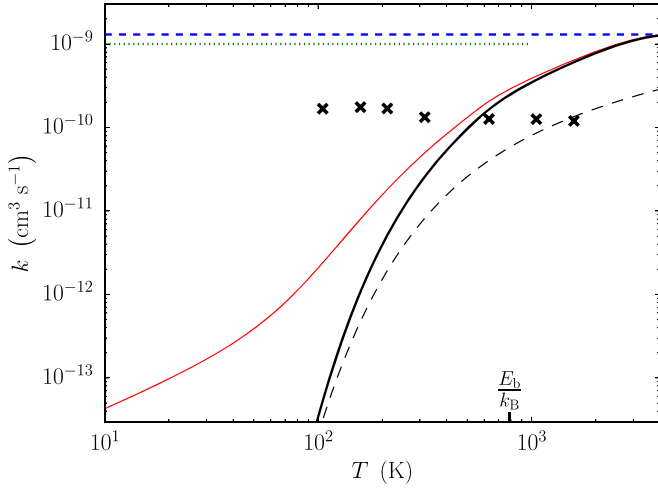


Figure 7. Rate coefficient, k , vs. temperature, T . Our model result from Equation (31) is shown by the black thick line for the thermal case and by the black thin long-dashed line for the translational case (i.e., $T_{\text{int}} = 0$ K). The tunneling-corrected thermal model from Equation (34) is shown by the red thin line. The black crosses plot the CT calculations of Moyano et al. (2004). The blue short-dashed line presents the Langevin rate coefficient from Equation (41). The green dotted line gives the rate coefficient commonly used in astrochemical models (Walmsley et al. 2004). Lastly, the energy of the reaction barrier, E_b/k_B , is indicated on the T axis by the vertical marker.

6.4.1. Model Rate Coefficients

Using our cross-section model, the thermal rate coefficient is given by

$$k_{\text{mod}}(T) = \left(\frac{8}{\pi \mu k_B^3 T^3} \right)^{1/2} \times \int_0^\infty \sigma_{\text{mod}}(E_r, \langle E_{\text{int}} \rangle) E_r \exp\left(\frac{-E_r}{k_B T} \right) dE_r, \quad (31)$$

where $T = T_{\text{gas}} = T_{\text{int}}$. The value of σ_{mod} is from Equation (30) using our best-fit values of $R_b = 2.53a_0$, $a = 0.3$, and $f = 0.2$. $\langle E_{\text{int}} \rangle$ is obtained from Equation (29).

The resulting thermal rate coefficient is shown in Figure 7 and given numerically in Table 5. The highest temperature presented corresponds to the thermal dissociation limit for H_3^+ (Kylänpää & Rantala 2011). This upper limit corresponds to $E_r = 0.34$ eV, which is well below $E_{\text{th}} = 1.65$ eV for the competing exoergic channels. Thus, the derived thermal rate coefficient is largely insensitive to the accuracy of the flux reduction factor $S(E_r, E_{\text{int}}, E_{\text{th}})$ of Equation (24).

As a self-consistency check, we also note that the thermal rate coefficient at $T_{\text{int}} = 1140$ K, corresponding to $\langle E_{\text{int}} \rangle = 0.185$ eV, is nearly equal to the measured merged-beams rate coefficient for $E_r = \langle E_{\text{int}} \rangle = 0.185$ eV. The thermal rate coefficient is $4.1 \times 10^{-10} \text{ cm}^3 \text{ s}^{-1}$ while the corresponding merged-beams rate coefficient is $\approx 3.7 \times 10^{-10} \text{ cm}^3 \text{ s}^{-1}$.

In order to enable ready implementation of our results into computational models, we have fit our model thermal rate coefficient with the commonly used Arrhenius–Kooij formula, giving

$$k_{\text{mod}}^{\text{fit}}(T[\text{K}]) = 4.55 \times 10^{-10} \left(\frac{T}{300} \right)^{0.5} \exp(-900/T) \text{ cm}^3 \text{ s}^{-1}. \quad (32)$$

Table 5
Experimentally Derived Rate Coefficients

T (K)	$k_{\text{tr}}(T)$	$k_{\text{mod}}(T)$ ($\text{cm}^3 \text{ s}^{-1}$) ^a	$k_{\text{tun}}(T)$
10.00	4.274[−14]
11.66	5.093[−14]
13.59	6.091[−14]
15.85	7.316[−14]
18.48	8.834[−14]
21.54	1.073[−13]
25.12	1.314[−13]
29.29	1.624[−13]
34.15	2.033[−13]
39.81	2.589[−13]
46.42	3.374[−13]
54.12	4.528[−13]
63.10	6.289[−13]
73.56	9.061[−13]
85.77	1.352[−12]
100.0	2.092[−14]	3.418[−14]	2.076[−12]
116.6	6.944[−14]	1.269[−13]	3.251[−12]
135.9	1.964[−13]	4.009[−13]	5.134[−12]
158.5	4.845[−13]	1.096[−12]	8.085[−12]
184.8	1.063[−12]	2.636[−12]	1.258[−11]
215.4	2.107[−12]	5.664[−12]	1.919[−11]
251.2	3.831[−12]	1.104[−11]	2.861[−11]
292.9	6.468[−12]	1.979[−11]	4.165[−11]
341.5	1.025[−11]	3.312[−11]	5.928[−11]
398.1	1.537[−11]	5.243[−11]	8.273[−11]
464.2	2.201[−11]	7.946[−11]	1.137[−10]
541.2	3.027[−11]	1.166[−10]	1.545[−10]
631.0	4.022[−11]	1.648[−10]	2.059[−10]
735.6	5.189[−11]	2.187[−10]	2.609[−10]
857.7	6.527[−11]	2.788[−10]	3.208[−10]
1000	8.034[−11]	3.465[−10]	3.876[−10]
1166	9.706[−11]	4.234[−10]	4.632[−10]
1359	1.154[−10]	5.106[−10]	5.489[−10]
1585	1.353[−10]	6.090[−10]	6.458[−10]
1848	1.568[−10]	7.186[−10]	7.536[−10]
2154	1.799[−10]	8.376[−10]	8.708[−10]
2512	2.046[−10]	9.618[−10]	9.930[−10]
2929	2.307[−10]	1.083[−9]	1.112[−9]
3415	2.582[−10]	1.190[−9]	1.216[−9]
3981	2.865[−10]	1.264[−9]	1.287[−9]

Note.

^a $a[-b] = a \times 10^{-b}$.

This fit is accurate to within 5% over the range $T = 100\text{--}4000$ K. The lower limit is where the rate coefficient is $\approx 3 \times 10^{-14} \text{ cm}^3 \text{ s}^{-1}$ and has been chosen as the rate coefficient rapidly decreases going to lower temperatures.

We have also calculated the translational temperature rate coefficient, k_{tr} , for the case where $T = T_{\text{gas}}$ and $T_{\text{int}} = 0$ K (i.e., $\langle E_{\text{int}} \rangle = 0$ eV). These data are plotted in Figure 7 and listed in Table 5.

6.4.2. Tunneling-corrected Thermal Rate Coefficient

In order to determine the influence of tunneling through the reaction barrier on the thermal rate coefficient for Reaction (1), we use the analytic approximation of Eckart (1930) as modified for an asymmetric barrier by Johnston (1966). The tunneling-corrected thermal rate coefficient can then be written as

$$k_{\text{tun}}(T) = \Gamma(T) k_{\text{mod}}(T). \quad (33)$$

Here, $\Gamma(T)$ is the tunneling-correction factor and can be expressed as

$$\Gamma(T) = \frac{1}{k_{\text{B}}T} \int_{-V_{\text{f}}}^{\infty} P(E_{\text{ts}}) \exp\left(\frac{-E_{\text{ts}}}{k_{\text{B}}T}\right) dE_{\text{ts}}, \quad (34)$$

where $P(E_{\text{ts}})$ is the tunneling probability (Miller 1979). The computed energy profile of the reaction and the corresponding normal mode frequencies of TS_3 , described in Section 4.3, provide a complete parameterization of the generalized Eckart potential, allowing us to express $P(E_{\text{ts}})$ in terms of the forward and reverse barrier heights (V_{f} and V_{r} , respectively) and the magnitude of the imaginary frequency, $\omega_{\text{b}} = |\omega_{\text{im}}|$ (which quantifies the width of the reaction barrier of the transition state). The quantity $E_{\text{ts}} = E_{\text{r}} + \langle E_{\text{int}} \rangle - V_{\text{f}}$ is the total reaction energy available to overcome the forward barrier of the transition state. The value of $P(E_{\text{ts}})$ can be evaluated as (Miller 1979)

$$P(E_{\text{ts}}) = \frac{\sinh(A)\sinh(B)}{\sinh^2\left(\frac{A+B}{2}\right) + \cosh^2(C)}, \quad (35)$$

with A , B , and C defined as

$$A = \frac{4\pi}{\hbar\omega_{\text{b}}}(E_{\text{ts}} + V_{\text{f}})^{1/2}(V_{\text{f}}^{-1/2} + V_{\text{r}}^{-1/2})^{-1}, \quad (36)$$

$$B = \frac{4\pi}{\hbar\omega_{\text{b}}}(E_{\text{ts}} + V_{\text{r}})^{1/2}(V_{\text{f}}^{-1/2} + V_{\text{r}}^{-1/2})^{-1}, \quad (37)$$

$$C = 2\pi\left(\frac{V_{\text{f}}V_{\text{r}}}{\hbar^2\omega_{\text{b}}^2} - \frac{1}{16}\right)^{1/2}. \quad (38)$$

For evaluation of the tunneling-corrected thermal rate coefficient, we use our theoretical results given in Section 4.3. There we find $V_{\text{f}} = E_{\text{b}} = 67.98$ meV and $V_{\text{r}} = E_{\text{b}} + |\Delta E_{\text{zp}}| = 125.78$ meV, based on the barrier height and the exoergicity of the exit channel given in Table 2. The value of $\omega_{\text{b}} = 875.9$ cm^{-1} is given in Table 3.

Figure 7 presents our tunneling-corrected thermal rate coefficient, which is also given numerically in Table 5. At the highest temperatures shown, the tunneling correction is unimportant and $k_{\text{tun}}(T)$ converges to $k_{\text{mod}}(T)$. As is expected, the correction increases with decreasing temperature. At $T = E_{\text{b}}/k_{\text{B}} = 789$ K, corresponding to the barrier energy, tunneling contributes $\approx 4 \times 10^{-17}$ $\text{cm}^3 \text{s}^{-1}$, or 17%, to the corrected thermal rate coefficient. Based on the work of Schwartz et al. (1998), we estimate that there is less than a factor of 2 uncertainty in the correction at this temperature. Going to lower temperatures, at $T = 75$ K, we find $k_{\text{tun}}(T) \approx 10^{-12}$ $\text{cm}^3 \text{s}^{-1}$ and at 10 K, $k_{\text{tun}} = 4.3 \times 10^{-14}$ $\text{cm}^3 \text{s}^{-1}$. Using the work of Schwartz et al. as a guide, we estimate that there is at least an order-of-magnitude uncertainty in our k_{tun} at these temperatures. Schwartz et al. showed that the accuracy of the $\Gamma(T)$ factor can be increased by fitting the Eckart potential function to the PES of the transition state. That level of theoretical complexity is beyond the scope of this paper.

Given the above caveats about the accuracy of the tunneling calculations, we have parameterized our results for $k_{\text{tun}}(T)$ in

units of $\text{cm}^3 \text{s}^{-1}$ as

$$k_{\text{tun}}^{\text{fit}}(T [\text{K}]) = \begin{cases} 3.3 \times 10^{-11} \left(\frac{T}{300}\right)^{2.73} \exp(28/T) & 10 \leq T < 180 \\ 3.0 \times 10^{-10} \left(\frac{T}{300}\right)^{0.64} \exp(-560/T) & 180 \leq T \leq 4000. \end{cases} \quad (39)$$

The accuracy of the fit is better than 18% over the given temperature ranges.

6.4.3. Comparison to Theoretical Rate Coefficients

In Figure 7, we compare to various theoretical rate coefficients for Reaction (1): the Langevin value, the value currently recommended by astrochemical modelers, and the CT result of Moyano et al. (2004). All three of these are only translational temperature rate coefficients, as they do not take into account any possible internal excitation of H_3^+ .

The Langevin rate coefficient is calculated by integrating $\sigma_{\text{L}}v_{\text{r}}$ over a Maxwell–Boltzmann distribution, yielding

$$k_{\text{L}} = 2\pi e \left(\frac{\alpha_{\text{D}}}{\mu}\right)^{1/2}. \quad (40)$$

This value is temperature independent. Taking into account that only three of the outgoing channels contribute to H_2D^+ formation, the Langevin rate coefficient for Reaction (1) is

$$k_{\text{L}} = 1.3 \times 10^{-9} \text{ cm}^3 \text{ s}^{-1}. \quad (41)$$

The Langevin value clearly overestimates the rate coefficient for this reaction at all temperatures of astrochemical relevance. Going to the high-temperature limit shown in Figure 7, $k_{\text{mod}}(T)$ converges to k_{L} . This is expected given our definition of the reaction cross section in Equation (27).

The rate coefficient recommended for astrochemical modeling appears to have originated with the work of Walmsley et al. (2004). Their value is

$$k_{\text{W}} = 1.0 \times 10^{-9} \text{ cm}^3 \text{ s}^{-1} \quad (42)$$

and is given for the temperature range of 10–1000 K. It is not clear how they derived this Langevin-like value, but their value clearly overestimates the rate coefficient at astrochemically relevant temperatures.

Lastly, we have used the CT results of Moyano et al. (2004) for ground-state H_3^+ to generate a translational temperature rate coefficient. We do this by multiplying their cross-section data, calculated for $T_{\text{int}} = 0$ K, by v_{r} and plotting their monoenergetic results at the temperatures given by $T = 2E_{\text{r}}/3k_{\text{B}}$. The results are nearly an order of magnitude below k_{L} and approximately constant with temperature. Compared to k_{mod} , the Moyano et al. results overestimate the rate coefficient at low temperatures. This is most likely due to the ZPE-leakage issue discussed in Section 6.3. At higher temperatures, ZPE leakage should cease to be an issue. At these temperatures, their results are, not surprisingly, significantly below k_{mod} , but they are in rough agreement with our results for k_{tr} .

6.5. Astrophysical Implications

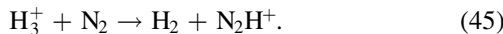
Our combined experimental and theoretical results indicate that Reaction (1) proceeds at prestellar core temperatures of $\sim 10\text{--}20\text{ K}$ with a rate coefficient of $\lesssim 10^{-13}\text{ cm}^3\text{ s}^{-1}$. This low rate coefficient arises from tunneling through a reaction barrier of $\approx 68\text{ meV}$. Given the height of this barrier, we expect that the magnitude of the rate coefficient will be insensitive to the ortho-to-para ratio of H_3^+ . The lowest energy level of ortho- H_3^+ lies only 2.8 meV above the lowest allowed level for para- H_3^+ (Hugo et al. 2009). This is an insignificant difference with respect to the reaction barrier energy.

Deuterated astrochemical models currently assume a rate coefficient for Reaction (1) of $\sim 1 \times 10^{-9}\text{ cm}^3\text{ s}^{-1}$ (Roberts & Millar 2000; Walmsley et al. 2004; Albertsson et al. 2013; Majumdar et al. 2017). These should be updated to use our results presented here, but we expect that the result will be to essentially turn off this channel for deuterating H_3^+ at prestellar core temperatures. Thus, current astrochemical models are likely to overestimate the H_2D^+ number density, $n(\text{H}_2\text{D}^+)$. In addition, this implies that HD is the primary species responsible for deuterating H_3^+ at these low temperatures (Hugo et al. 2009; Albertsson et al. 2013; Sipilä et al. 2017) via



This reaction is barrierless and exoergic by 19.98 meV for the reactants and products in their lowest energy states (Ramanlal & Tennyson 2004; Hugo et al. 2009). We are unaware of any publicly available deuterated astrochemical models and so our discussions here are purely qualitative.

Our current understanding of collapsing low- and high-mass prestellar cores may also be affected by Reaction (1) being essentially closed below 20 K . Ground-based observations of the deuterium fractionation ratio $D_{\text{frac}}^{\text{N}_2\text{H}^+} \equiv n(\text{N}_2\text{D}^+)/n(\text{N}_2\text{H}^+)$ are used as a chemical clock for comparing to dynamical models of core formation and evolution (Kong et al. 2015). These two ions are predicted to form primarily from the reactions



Deuterium fractionation increases with time as a core begins to collapse. It then decreases once a protostar forms and begins to heat the gas, enabling the endoergic reverse of Reaction (43) to take place, thereby reducing the formation of N_2D^+ .

Kong et al. (2015) reported that values of $D_{\text{frac}}^{\text{N}_2\text{H}^+} \gtrsim 0.1$ are commonly observed in low- and high-mass prestellar cores. These values imply chemical timescales longer than the local freefall timescale given by simple gravitational collapse models. Kong et al. posited that this is indirect evidence that magnetic fields play an important role in regulating the evolution and collapse of prestellar cores, and thereby of star formation. Given that Reaction (1) is essentially closed, reducing the H_2D^+ abundance, this implies that even longer chemical timescales are required to match the observed values of $D_{\text{frac}}^{\text{N}_2\text{H}^+}$. If this is the case, then that strengthens the argument of Kong et al.

7. Summary

We have reported here a combined experimental and theoretical study of atomic D reacting with H_3^+ , leading to

the formation of H_2D^+ . Our findings indicate that this reaction is essentially closed at the $\sim 10\text{--}20\text{ K}$ temperatures of astrochemical relevance. We have presented thermal rate coefficients so that deuterated astrochemical models can be readily updated accordingly.

The authors thank Evelyne Roueff and Fabrice Dayou for stimulating conversations. This research was supported, in part, by the NSF Division of Astronomical Sciences Astronomy & Astrophysics Grants program under AST-1613267. P.-M.H. was supported, in part, by the Deutsche Forschungsgemeinschaft (DFG) under grant No. HI 2009/1-1. J.L. thanks the ULB/VUB computing center and the Consortium des Equipements de Calcul Intensif (FRS-FNRS and Walloon Region) for computational support. X.U. is a Senior Research Associate of the Fonds de la Recherche Scientifique-FNRS and acknowledges travel support from Fonds de la Recherche Scientifique-FNRS through IISN grant No. 4.4504.10.

Software: Molpro (Werner et al. 2012, 2015).

ORCID iDs

P.-M. Hillenbrand  <https://orcid.org/0000-0003-0166-2666>
 K. P. Bowen  <https://orcid.org/0000-0003-2483-8863>
 X. Urbain  <https://orcid.org/0000-0003-3326-8823>
 D. W. Savin  <https://orcid.org/0000-0002-1111-6610>

References

- Adams, N. G., & Smith, D. 1981, *ApJ*, **248**, 373
 Aikawa, Y., Wakelam, V., Hersant, F., Garrod, R. T., & Herbst, E. 2012, *ApJ*, **760**, 40
 Albertsson, T., Semenov, D. A., Vasyunin, A. I., Henning, T., & Herbst, E. 2013, *ApJS*, **207**, 27
 Alijah, A., & Varandas, A. J. C. 2008, *JChPh*, **129**, 034303
 Álvarez-Collado, J. R., Aguado, A., & Paniagua, M. 1995, *JChPh*, **102**, 5725
 Bhowmick, S., Bossion, D., Scribano, Y., & Suleimanov, Y. V. 2018, *PCCP*, **20**, 26752
 Brouillard, F., & Claeys, W. 1983, in *Physics of Ion-Ion and Electron-Ion Collisions*, ed. F. Brouillard & J. W. McGowan (New York: Plenum), 415
 Bruhns, H., Kreckel, H., Miller, K., et al. 2010a, *RSci*, **81**, 013112
 Bruhns, H., Kreckel, H., Miller, K. A., Urbain, X., & Savin, D. W. 2010b, *PhRvA*, **82**, 042708
 Brünken, S., Sipilä, O., Chambers, E. T., et al. 2014, *Natur*, **516**, 219
 Caselli, P., van der Tak, F. F. S., Ceccarelli, C., & Bacmann, A. 2003, *A&A*, **403**, L37
 Caselli, P., Vastel, C., Ceccarelli, C., et al. 2008, *A&A*, **492**, 703
 de Ruette, N., Miller, K. A., O'Connor, A. P., et al. 2016, *ApJ*, **816**, 31
 Dunning, T. H., Jr. 1989, *JChPh*, **90**, 1007
 Eckart, C. 1930, *PhRv*, **35**, 1303
 Flower, D. R., Pineau Des Forêts, G., & Walmsley, C. M. 2006, *A&A*, **449**, 621
 Friesen, R. K., Di Francesco, J., Bourke, T. L., et al. 2014, *ApJ*, **797**, 27
 Friesen, R. K., Di Francesco, J., Myers, P. C., et al. 2010, *ApJ*, **718**, 666
 Gerlich, D., Herbst, E., & Roueff, E. 2002, *P&SS*, **50**, 1275
 Gerlich, D., & Schlemmer, S. 2002, *P&SS*, **50**, 1287
 Giles, K., Adams, N. G., & Smith, D. 1992, *JPhCh*, **96**, 7645
 Grenier, I. A., Black, J. H., & Strong, A. W. 2015, *ARA&A*, **53**, 199
 Guo, Y., Thompson, D. L., & Sewell, T. D. 1996, *JChPh*, **104**, 576
 Habershon, S., Manolopoulos, D. E., Markland, T. E., & Miller, T. E., III 2013, *ARPC*, **64**, 387
 Harju, J., Haikala, L. K., Lehtinen, K., et al. 2006, *A&A*, **454**, L55
 Huber, K., & Herzberg, G. 1979, *Molecular Spectra and Molecular Structure: Constants of Diatomic Molecules*, Vol. IV (Boston, MA: Springer)
 Hugo, E., Asvany, O., & Schlemmer, S. 2009, *JChPh*, **130**, 164302
 Jankunas, J., Sneha, M., Zare, R. N., et al. 2014, *PNAS*, **111**, 15
 Jaquet, R. 2013, *MoPh*, **111**, 2606
 Jiang, G., Wang, H. Y., & Zhu, Z. H. 1989, *CPL*, **91**, 267
 Johnston, H. S. 1966, *Gas Phase Reaction Rate Theory* (New York: Ronald Press Co.), 37
 Kendall, R. A., Dunning, T. H., & Harrison, R. J. 1992, *JChPh*, **96**, 6796

- Knowles, P. J., & Werner, H.-J. 1985, *CPL*, **115**, 259
- Knowles, P. J., & Werner, H.-J. 1988, *CPL*, **145**, 514
- Kong, S., Caselli, P., Tan, J. C., Wakelam, V., & Sipilä, O. 2015, *ApJ*, **804**, 98
- Kramida, A., Ralchenko, Y., Reader, J. & NIST ASD Team 2018, NIST Atomic Spectra Database (ver. 5.5.6) (Gaithersburg, MD: National Institute of Standards and Technology), <https://physics.nist.gov/asd>
- Kreckel, H., Bruhns, H., Čížek, M., et al. 2010, *Sci*, **329**, 69
- Kreckel, H., Novotný, O., Crabtree, K. N., et al. 2010, *PhRvA*, **82**, 042715
- Kylänpää, I., & Rantala, T. T. 2011, *JChPh*, **135**, 104310
- Lee, J.-E., & Bergin, E. A. 2015, *ApJ*, **799**, 104
- Lee, K. L. K., Quinn, M. S., Kolmann, S. J., Kable, S. H., & Jordan, M. J. T. 2018, *JChPh*, **148**, 194113
- Levine, R. D. 2005, *Molecular Reaction Dynamics* (Cambridge: Cambridge Univ. Press)
- Lie, G. C., & Frye, D. 1992, *JChPh*, **96**, 6784
- Linstrom, P. J., & Mallard, W. G. (ed.) 2018, NIST Chemistry WebBook, NIST Standard Reference Database 69 (Gaithersburg MD: National Institute of Standards and Technology), doi:10.18434/T4D303
- Lu, D., & Hase, W. L. 1989, *JChPh*, **91**, 7490
- Majumdar, L., Gratier, P., Ruaud, M., et al. 2017, *MNRAS*, **466**, 4470
- McElroy, D., Walsh, C., Markwick, A. J., et al. 2013, *A&A*, **550**, A36
- McLaughlin, B. M., Stancil, P. C., Sadeghpour, H. R., & Forrey, R. C. 2017, *JPhB*, **50**, 114001
- Mielke, S. L., Schwenke, D. W., & Peterson, K. A. 2005, *JChPh*, **122**, 224313
- Millar, T. J., Bennett, A., & Herbst, E. 1989, *ApJ*, **340**, 906
- Miller, K. A., Bruhns, H., Čížek, M., et al. 2012, *PhRvA*, **86**, 032714
- Miller, K. A., Bruhns, H., Eliášek, J., et al. 2011, *PhRvA*, **84**, 052709
- Miller, W. H. 1979, *JChS*, **101**, 6810
- Morong, C. P., Gottfried, J. L., & Oka, T. 2009, *JMoSp*, **255**, 13
- Moyano, G. E., Pearson, D., & Collins, M. A. 2004, *JChPh*, **121**, 12396
- O'Connor, A. P., Grussie, F., Bruhns, H., et al. 2015a, *RSci*, **86**, 113306
- O'Connor, A. P., Urbain, X., Stützel, J., et al. 2015b, *ApJ*, **219**, 6
- O'Hanlon, J. F. 2003, *A User's Guide to Vacuum Technology* (Hoboken, NJ: Wiley)
- Pagani, L., Lesaffre, P., Jorfi, M., et al. 2013, *A&A*, **551**, A38
- Pagani, L., Vastel, C., Hugo, E., et al. 2009, *A&A*, **494**, 623
- Pavanello, M., Adamowicz, L., Alijah, A., et al. 2012, *JChPh*, **136**, 184303
- Phelps, A. V. 1992, *JPCRD*, **21**, 883
- Pillai, T., Caselli, P., Kauffmann, J., et al. 2012, *ApJ*, **751**, 135
- Ramanlal, J., & Tennyson, J. 2004, *MNRAS*, **354**, 161
- Rienstra-Kiracofe, J. C., Tschumper, G. S., Schaefer, H. F., Nandi, S., & Ellison, G. B. 2002, *ChRv*, **102**, 231
- Roberts, H., & Millar, T. J. 2000, *A&A*, **361**, 388
- Rodgers, S. D., & Millar, T. J. 1996, *MNRAS*, **280**, 1046
- Sanz-Sanz, C., Roncero, O., Paniagua, M., & Aguado, A. 2013, *JChPh*, **139**, 184302
- Schwartz, M., Marshall, P., Berry, R. J., Ehlers, C. J., & Petersson, G. A. 1998, *JPhChA*, **102**, 10074
- Schwerdtfeger, P., & Nagle, J. K. 2019, *MolPh*, **117**, 1200
- Seely, D., Bruhns, H., Savin, D., et al. 2008, *NIMPA*, **585**, 69
- Sipilä, O., Caselli, P., & Harju, J. 2013, *A&A*, **554**, A92
- Sipilä, O., Harju, J., & Caselli, P. 2017, *A&A*, **607**, A26
- Stark, R., van der Tak, F. F. S., & van Dishoeck, E. F. 1999, *ApJL*, **521**, L67
- Strömholm, C., Schneider, I. F., Sundström, G., et al. 1995, *PhRvA*, **52**, R4320
- Swift, J. J. 2009, *ApJ*, **705**, 1456
- van der Tak, F. F. S. 2006, *RSPTA*, **364**, 3101
- Vastel, C., Caselli, P., Ceccarelli, C., et al. 2006, *ApJ*, **645**, 1198
- Vastel, C., Phillips, T. G., & Yoshida, H. 2004, *ApJL*, **606**, L127
- Walmsley, C. M., Flower, D. R., & Pineau des Forêts, G. 2004, *A&A*, **418**, 1035
- Werner, H.-J., & Knowles, P. J. 1985, *JChPh*, **82**, 5053
- Werner, H.-J., & Knowles, P. J. 1988, *JChPh*, **89**, 5803
- Werner, H.-J., Knowles, P. J., Knizia, G., et al. 2015, MOLPRO, version 2015.1, a package of ab initio programs, Cardiff, UK
- Werner, H.-J., Knowles, P. J., Knizia, G., Manby, F. R., & Schütz, M. 2012, *WIREs Comput. Mol. Sci.*, **2**, 242